Aparicio Esteve, E., Hernández Alonso, A., Ureña Ureña, J. & Villadangos Carrizo, J.M. 2020, "Visible light positioning system based on a quadrant photodiode and encoding techniques", IEEE Transactions on Instrumentation and Measurement, vol. 69, no. 8, pp. 5589-5603.

Available at http://dx.doi.org/10.1109/TIM.2019.2962563

# Visible Light Positioning System based on a Quadrant Photodiode and Encoding Techniques

Elena Aparicio-Esteve, Álvaro Hernández, *Senior Member, IEEE*, Jesús Ureña, *Senior Member, IEEE*, José M. Villadangos

***Abstract*—Visible Light Positioning Systems (VLPS) are a feasible alternative to local positioning systems thanks to the technology improvement and massive use of Light Emitting Diodes (LED). Compared to other technologies, VLPSs can provide significant advantages, such as the achieved accuracy, although they still present some issues, mainly related to the reduced coverage area or the high computational load. This work proposes the design of a VLPS based on four LED lamps as transmitters and a Quadrant Photodiode Angular Diversity Aperture (QADA) as a receiver. As the shape of the QADA is circular and the aperture to be installed over it is square, we derive the corresponding general equations to obtain the currents through the different pads of the QADA, regarding the angle of incidence of the light (and, inversely, how to estimate the angle of incidence from the measured currents). An encoding scheme based on 1023-bit Kasami sequences is proposed for every transmission from the LED lamps, thus providing multiple access capability and robustness against low signal-noise ratios and harsh conditions, such as multipath and near-far effect. A triangulation technique has been applied to estimate the receiver's position, by means of the *Least Squares Estimator* (LSE), together with some geometrical considerations. The proposal has been validated by simulation and by experimental tests, obtaining 3D positioning average errors below 13 cm and 5.5 cm for separations between the transmitters' plane and the receiver of 2 m and 1 m, respectively.**

***Index Terms*— *Angle-of-Arrival* (AOA), Quadrant Photodiode, LED lamps, *Visible Light Positioning* (VLP).**

## I. Introduction

The need for affordable and accurate positioning systems is highly increasing due to the development of a variety of applications and services based on positioning. Although the *Global Navigation Satellite Systems* (GNSS) are the most used nowadays, their use is mainly limited to outdoor environments, obtaining good results in not densely populated areas. Other positioning systems, such as WiFi [1] [2], Bluetooth [3] or radar [4], overcome weaknesses from GNSS in areas where its precision decreases. Related to Local Positioning Systems (LPS), it can be distinguished those based on optical, mechanical, acoustic and radiofrequency technologies, among others [5]. Mechanical positioning systems are those mainly based on Inertial Measurement Unit (IMU) and they are usually combined with other positioning systems [6]. Their main advantages are their small size and low cost, but affected by stability and drifts [7]. On the other hand, acoustic positioning systems use sound or ultrasounds to estimate position, often with an accuracy in the range of centimetres [8]. Radiofrequency systems allow the user to obtain the position by using any radio signal (WiFi; RFID, *Radio Frequency Identification*; UWB, *Ultrawide Band*; LTE, *Long-Term Evolution*;…) [9], with accuracies that go from several meters to centimetres in particular situations and applications [5]. Their indoor use is highly spread due to its implementation on the already installed infrastructure. Lately, positioning systems based on optical systems are those working within the visible light or infrared spectrum [10]. There is an interest in this technology due to its low cost, long lifetime and easy manipulation and integration on the workplace [11], in addition to its harmless [12]. Several previous works have already used hybrid techniques, thus combining Visible Light Positioning Systems (VLPS) with ultrasounds [13] or WiFi [14], among others, to bring robustness and accuracy to the link.

VLPS are used both in indoor and outdoor areas. In general, the vast majority of previous works are focused on indoor positioning due to the high influence from the ambient light on this type of systems [12]. In the case of indoor positioning, whereas the transmitter is usually a lamp or a LED (*Light Emitting Diode*) array, it can be distinguished positioning systems based on imaging sensors and on photodetectors at the receiver. Positioning systems based on imaging sensors typically use the camera of conventional smartphones [15] or CMOS cameras [16] [17] [18]. Nonetheless, they require complex image processing algorithms that slow down the positioning computation [19]. On the other hand, positioning systems, whose receptor is a photodetector, use photodiodes [20] [21] or an array of photodiodes [22] [23], to generate a current corresponding to a light impact, from which it is possible to estimate the receiver's position. *Position-sensitive detectors* (PSD) in combination with lens and *Quadrant Photodiode Angular Diversity Aperture* (QADA) with an aperture are the main receiving systems employed in visible and infrared light detection. The use of a QADA [22] is highlighted due to its better angle diversity. In [22] a square aperture whose projection equals a square circumscribed in the photoreceiver is

This work has been supported by the Spanish Ministry of Science, Innovation and Universities (SOC-PLC project, ref. TEC2015-64835-C3-2-R, TARSIUS project, ref. TIN2015-71564-C4-1-R, and the Youth Employment Program PEJ2018-003459-A).

Elena Aparicio-Esteve, Álvaro Hernández, Jesús Ureña and José M. Villadangos are with Electronics Department, University of Alcalá, Alcalá de Henares (Madrid), Spain (e-mail: {elena.aparicio, alvaro.hernandez, jesus.urena, jm.villadangos}@uah.es).

chosen in order to simplify the mathematical problem approached in this work. PSD systems have the drawback that the PSD width must be increased as the desired working distance increases, therefore their working area is typically below 1 metre [24]. It is worth mentioning that in [25] [26] a receiver system combining a camera with a QADA receiver was proposed, achieving errors around 20 cm in simulation in a similar scenario as the one proposed hereinafter. The work presented here also involves an experimental verification of the proposal, as well as its improvement by applying encoding techniques that allow average errors below 7 cm to be achieved with a single receiver at a distance of 2 m from transmitters.

On the other hand, the most used positioning techniques are triangulation or trilateration/multilateration with *Time-of-Flight* (TOF) measures (or with TOA*, Times-of-Arrival*; TDOA, *Time-Difference-of-Arrival*) [21], *Received Signal Strength* (RSS) [27] [28], or *Angle-of-Arrival* (AOA) [11]. Sometimes, other methods such as proximity ones are also involved [29]. Main drawbacks regarding TOF measures are the required synchronization and the high value of the light velocity, which implies that 1 ns time estimation error becomes a 30 cm positioning error [17]. That is the reason why TOFs are mainly used in optics for long distances (> 50 m) [24]. Positioning using RSS must consider light reflections in all surfaces and the multipath effect, thus increasing the difficulty of the algorithms [28]. Actually, RSS is used for short distances in optics (from a few millimetres up to about 50 mm) [19]. Finally, the positioning algorithms based on AOA estimate the angle of arrival coming from the LEDs. Their main advantage is that they only require three measures to obtain a position in a three-dimension (3D) space, as well as no synchronization is needed between transmitters [28].

Another key aspect is the medium access technique, often related to the modulation scheme implemented in transmissions. Several works rely on *On-Off Keying* (OOK) modulations [30] [31], due to its simplicity [32]; whereas others use *Pulse Position Modulation* (PPM) [33] [34], since *Pulse Width Modulation* (PWM) and PPM are the most robust modulation against *Inter-Symbol Interference* (ISI). On the other hand, in [35] a BPSK (*Binary Phase Shift Keying*) is compared with an OOK modulation, resulting in the BPSK to have the best performance for visible light communications. Furthermore, the encoding of visible light signals involves different types of binary sequences [36]: Gold [37] and Walsh-Hadamard [38] [39] sequences, among others. Reed-Solomon codes [40] dedicated to decrease the influence from the multipath effect and the ISI; Double Binary Turbo codes [41] implemented to reduce information losses caused by optical noise in fluorescent lamps; Reed-Muller codes [42] used for accurate dimming control in OOK; or Polar codes [43] are some examples.

This work presents an Indoor Visible Positioning System, which is based on four LED lamps as transmitters and a QADA as a receiver. A triangulation technique has been proposed to estimate the receiver's position inside the corresponding coverage area. As the shape of the receiver is circular and the aperture used over it is square, general equations have been derived to obtain the currents through the different pads, regarding the angle of incidence of the light (and, inversely, to estimate the angle of incidence from the measured currents). Additionally, one of the main novelties of the proposal is the use of an encoding scheme based on 1023-bit Kasami sequences. This has been proposed for every transmission coming from the LED lamps, in order to provide multiple access capability (simultaneous transmissions from the LED lamps), as well as the improvement of the system to deal with very low signal to noise ratios, with different types of noise, and with adverse conditions, such as multipath and near-far effect. The proposal has been evaluated and successfully verified by means of simulations and experimental implementation. Therefore, the main contribution of the proposal is the design and implementation of a robust VLPS, when encoding techniques have been applied to improve the positioning performance, achieving experimental results consistent with the previous theoretical analysis.

The rest of the manuscript is organized as follows: Section II provides a description of the LED emitters and the proposed photodiodes matrix; Section III details the designed encoding technique and the propagation model; Section IV deals with the proposed positioning algorithm; Section V shows some experimental results; and, finally, conclusions are discussed in Section VI.

## II. Global Overview of the Proposed VLPS

The proposed VLPS is based on a set of four emitters/LED lamps, which are placed at certain points, so that they cover a common area where a receiver can detect all their emissions and estimate its own position. A general scheme of the VLPS is shown in Fig. 1, whereas the details of the receiver are zoomed in Fig. 2.a).

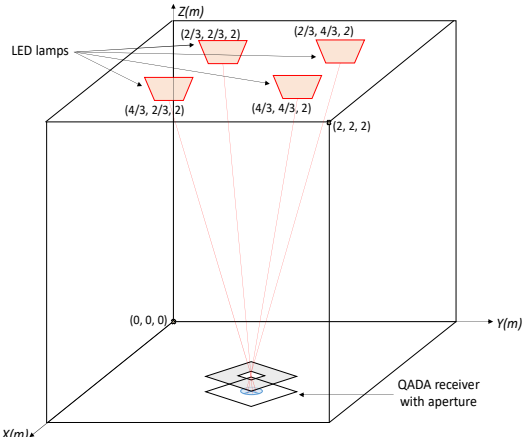


Fig. 1. Proposed positioning system with LED emitters and a photodiode array (note that elements are not to scale).

The four LED emitters involved hereinafter are composed of five modules OVM12F3W7 (white, typical illumination 4 lx at 1 m and 1 lx at 2 m, 5000-7000 K) [44] connected in parallel; each module has three LEDs in series. With a beam angle of $\beta$=120º, they emit 7.5 W whether a typical voltage of 12 V is applied. Those LED modules are excited individually with a particular 1023-bit Kasami code, which is BPSK (Binary Phase Shift Keying) modulated with a square carrier signal. This code $c_i$ is transmitted to the LED lamps $i$ by using a Blueboard LPC1768-H platform. On the other hand, the receiver uses a QP50-6-18u-SD2 board [45]. It has a QADA receiver QP50-6-18u-TO8 with a radius $r$ = 3.9 mm, where each photodiode has

an effective area of 11.78 mm$^2$. It provides bottom minus top ($Y$ axis), left minus right ($X$ axis) difference signals, and the sum of all four quadrant diode signals. Its responsivity at a wavelength $\lambda$ = 625 nm is 0.4 A/W and the theoretical noise is 15 nV/√Hz with a 15 V input signal. A square aperture made by 3-D printing has been added to the photodiode array, with a side equal to the diameter of the photoreceiver circle ($2 \cdot r$=7.8mm) and installed at a height $h_{ap}$ = 2.6 mm above it, as can be observed in Fig. 2.a). The shape of the aperture has been chosen to simplify the equations to estimate the angle of incidence (compared to a circular aperture, for instance), and the length has been established so that all the photoreceiver area is covered.

In addition, there is a tradeoff between maximizing the useable area in the QADA receiver while maximizing the whole coverage volume. The positions of the LED lamps $i$ are set to cover the largest possible area for a certain space. As a study case, the proposed system has been particularized hereinafter for a volume of 2 x 2 x 2 m$^3$, where the LED lamps, $i$={1,2,3,4}, have been placed at the coordinates ($x_{t,i}$, $y_{t,i}$, $z_{t,i}$) defined in Table I. Note that two reference systems are considered in this proposal: one to refer the impact point of the light onto the surface of the quadrant receiver ($x_r$, $y_r$); and the other regarding the position of the receiver in the whole volume ($x$, $y$, $z$).

Concerning the system characterization, for the analysis and measurements conducted in this work, it is considered that the receiver and the transmitter $i$ are accurately aligned from an angular point of view, so there is no angle of rotation or inclination (neither in the transmitting LEDs nor in the QADA). Furthermore, it is assumed that the $X$ and $Y$ axes of the LED $i$ and the QADA receiver are aligned. In addition, in order to position the receiver, at least three impact points must be available in the QADA receiver.

Note that in practical applications, some or even all these constraints must be released. For instance, the system can be used in its current configuration as a 3D positioning system that can be applied to obtain the "pose" (position and orientation in the $X$-$Y$ plane) of a mobile robot, with the only constraint that it must move on a horizontal floor. The estimation of the polar angle can be done mathematically by the calculation of the angle that the receiver (still horizontal) should be rotated to put the four incident points in a rectangular shape aligned with the own axis of the receiver. Once the polar angle has been estimated and the rotation compensated, all the algorithm proposed here can be applied to obtain the coordinates ($x$, $y$, and $z$). A brief introduction about this point has been included in Appendix B and derived in [46]. Further improvements regarding rotations in more axes can be also derived, but at the cost of using more receivers.

TABLE I
LED LAMPS COORDINATES IN THE STUDY CASE CONSIDERED HERE

| LED | Coordinates ($x_{t,i}$, $y_{t,i}$, $z_{t,i}$) |
|---|---|
| LED 1 | (4/3 m, 2/3 m, 2 m) |
| LED 2 | (4/3 m, 4/3 m, 2 m) |
| LED 3 | (2/3 m, 4/3 m, 2 m) |
| LED 4 | (2/3 m, 2/3 m, 2 m) |

## III. PROPOSED CENTRAL IMPACT POINT ESTIMATION AT THE RECEIVER

The operation principle of the proposal is based on the fact that the light coming from the emitters goes through the centre of the square aperture placed on the receiver and lights the array of photodiodes (see Fig. 2.a). The coordinates ($x_r$, $y_r$) of the impact point of the incident ray at the surface of the QADA receiver allows the angle of incidence $\psi$ of the beam to be geometrically estimated (see Fig. 2.b), by taking into account the corresponding geometrical considerations about the aperture height $h_{ap}$, as denoted in (1) and (2).

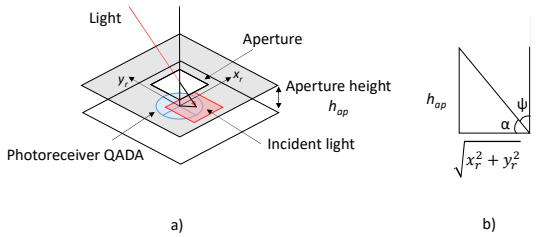


Fig. 2. a) Incident light in the photoreceiver QADA; b) Geometrical analysis of the aperture and the impact point.

$$\alpha = tan^{-1}\left(\frac{h_{ap}}{\sqrt{x_r^2 + y_r^2}}\right) \quad (1)$$

$$\psi = 90^{o} - \alpha \quad (2)$$

Where $\alpha$ is the angle at which the beam reaches the receiver; $\psi$ is the angle at which the light beam passing through the centre of the aperture impacts on the array of photodiodes (see Fig. 2.b); $x_r$ and $y_r$ are the coordinates of the impact point at the receiver; and $h_{ap}$ is the height at which the square aperture is installed.

In order to achieve a higher resolution, a full usage of the area of the photodiodes is required, thus, the side of the square aperture is set equal to the diameter of the photoreceptor (see Fig. 2.a and Fig. 3). In this way, when the center of the light beam impacts at the coordinates ($x_r$= 0, $y_r$ = 0), QADA's center, all the area from the four quadrants is lighted on.

According to the incidence angle $\psi$, different areas are illuminated in the four photodiodes that constitute the receiver. Fig. 3 shows the four quadrants and the area covered by the beam of light that passes through the aperture for the case of an incident ray at the impact point ($x_r$, $y_r$) [22]. The incident light generates four different currents $i_j(t)$ for every quadrant $j$={1,2,3,4}.

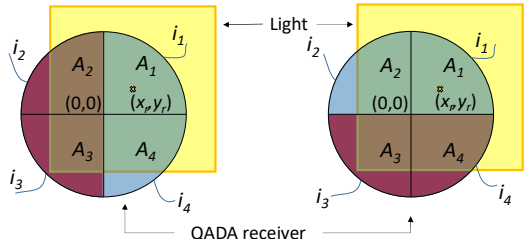


Fig. 3. Incident light in a QADA receiver through an aperture for both coordinates: $X$ axis (left) and $Y$ axis (right).

With no noise, the currents $i_j(t)$ generated by each quadrant $j$ can be considered proportional to the lighted areas $A_j(t)$ from

the different quadrants. In this way, the ratios $p_x(t)$ and $p_y(t)$ can be defined as a function of the areas $A_j(t)$ from every quadrant $j$, as denoted in (3) and (4).

$$p_x(t) = \frac{A_2(t) + A_3(t) - A_1(t) - A_4(t)}{A_1(t) + A_2(t) + A_3(t) + A_4(t)} = \frac{V_{LR}(t)}{V_{sum}(t)}, \forall x \quad (3)$$

$$p_y(t) = \frac{A_3(t) + A_4(t) - A_1(t) - A_2(t)}{A_1(t) + A_2(t) + A_3(t) + A_4(t)} = \frac{V_{BT}(t)}{V_{sum}(t)}, \forall y \quad (4)$$

Where $V_{sum}(t) = \sum_{j=1}^{4} v_j(t)$; $V_{LR}(t) = \big(v_2(t) + v_3(t)\big) - \big(v_1(t) + v_4(t)\big)$; and $V_{BT}(t) = \big(v_3(t) + v_4(t)\big) - \big(v_1(t) + v_2(t)\big)$ [45]. Note that these output voltages provided by the QADA receiver are the combination of the currents $i_j(t)$ obtained by the different photodiodes, transformed into the voltages $v_j(t)$ by means of a transimpedance amplifier, as detailed in the Appendix A.

Hereinafter it is assumed that the transmitter follows a Lambertian radiation pattern [47], typical of LEDs. It is worth nothing that the orientation of the LEDs and the receiver has also been considered. In our case, LEDs are oriented so that their maximum emitted intensity is perpendicular to the plane where they are placed and in the direction of the receiver plane. The general expression for the DC channel gain of each quadrant $j$ is given by (5) [47].

$$H_j = \frac{A_j \cdot (m+1)}{d^2 \cdot 2 \cdot \pi} \cdot \cos^m(\phi) \cdot \mathrm{T_s}(\psi) \cdot \mathrm{g}(\psi) \cdot \cos(\psi) \quad (5)$$

Where $m$ is the Lambertian order of the LED $i$; $A_j$ is the area of the $j^{th}$ quadrant; $d$ is the distance between the transmitter and the receiver; $\psi$ and $\phi$ are the incident and emergence angles, respectively; $T_s(\psi)$ is the signal transmission of the filter; and $g(\psi)$ is the concentrator gain. The channel gain can be restricted to the particular case considered here, where there is neither concentrator nor filter, and neither the transmitter nor the receivers are tilted ($\phi = \psi$) (6).

$$H_j = \frac{A_j \cdot (m+1)}{d^2 \cdot 2 \cdot \pi} \cdot \cos^{m+1}(\phi) \quad (6)$$

The coverage volume particularized for a beam angle $\beta$=120º in the transmitters is plotted in Fig. 4. The condition for a position to be considered in the coverage map is that at least three LED lamps are available/visible in that position. This condition is met for all the positions below the surface depicted in Fig. 4.a). Black lines in Fig. 4 remarks the coverage area at planes $z$ = 0.5 m, 1 m, 1.5 m in $XY$ and black crosses represent the projection of the transmitters' positions.

Since the proposal is based on the ratios between the four quadrants of the QADA, it is expected that external factors, such as temperature or aging, affect similarly all of them, therefore discarding them. With regard to possible obstacles avoiding desirable LOS (Line-of-Sight) situations, note that, either the obstacle should cover at least two LEDs (if only one LED is hidden, there are still three points of incidence available, and an estimation of the receiver's position can be done), or it should imply a specular reflection, thus deviating the path of the light onto a false point of incidence ($x_r$, $y_r$) in the QADA.

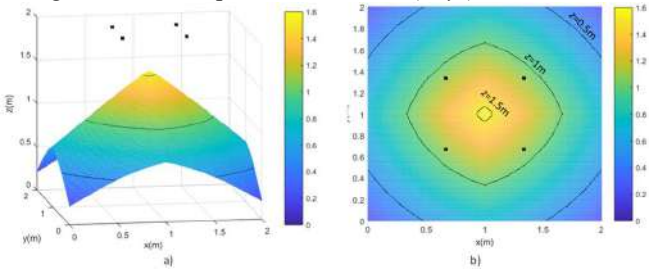


Fig. 4. Coverage volume particularized for a beam angle $\beta$ = 120º in the four transmitters: a) General overview of the volume; b) Coverage area at planes $z$=0.5 m, 1 m, 1.5 m in $XY$.

### A. *Coding and signal processing*

The channel gain is influenced by the modulation involved, as well as by the encoding techniques applied to transmissions. As mentioned before, in this proposal, 1023-bit Kasami sequences are transmitted by means of a BPSK modulation, with a square carrier to facilitate an ON/OFF operation of the LEDs. To eliminate the effect of flickering with its consequent negative effects on health [48], a much higher carrier frequency than 200 Hz has been fixed. The BPSK carrier frequency is actually $f_c$ = 25 kHz, whereas the sampling frequency is fixed ten times higher, $f_s$ = 250 kHz (oversampling $M = f_s/f_c$ = 10). Four Kasami sequences $c_i$ have been assigned (each for a particular LED $i$). Note that every quadrant $j$ will have the contributions from all the signals modulated with sequences $c_i$ transmitted by all the LEDs. The sequences $c_i$ are simultaneously emitted by every LED $i$, with a displacement of 5 samples (half modulation symbol $M$/2) with respect to the previous one, so that the LED $i$ = 4 transmitting the fourth Kasami code $c_4$ has a displacement of a symbol and a half with respect to the LED $i$ = 1 transmitting the first code $c_1$. Note that the modulation symbol length is $M$ = 10 samples. These displacements of sequences are intended to improve the cross-

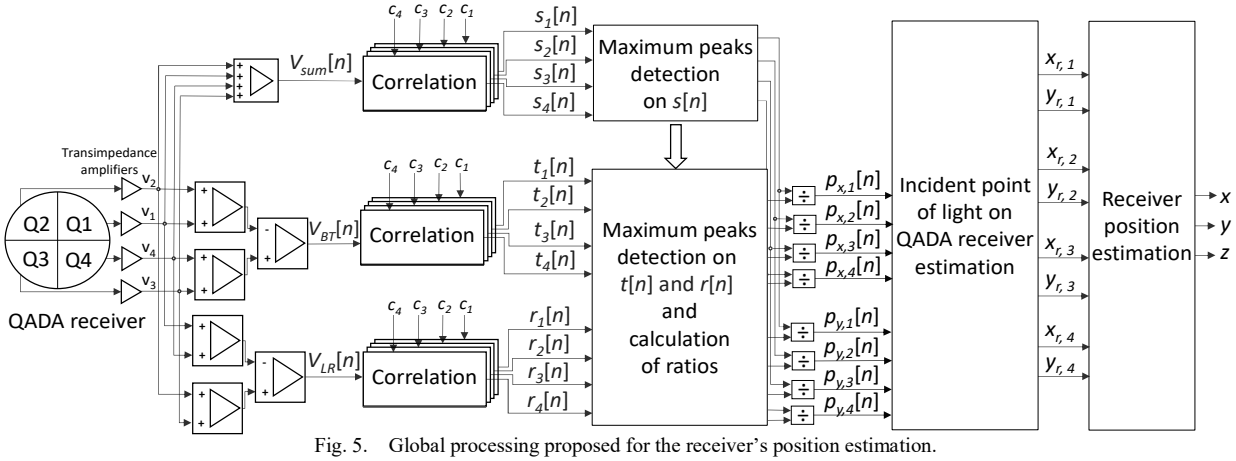


Fig. 5. Global processing proposed for the receiver's position estimation.

correlation properties of transmissions at the receiver, since it can be assumed that the times-of-arrival are the same for all the emissions. Furthermore, the displacements included in the emissions are also found at the reception.

Fig. 5 details the global processing proposed for the final receiver's position estimation. As can be observed, after the signals are detected by the QADA receiver, they are correlated with the above-mentioned Kasami sequences $c_i$, so that different peaks are obtained and processed to calculate the ratios $p_{x,i}[n]$ and $p_{y,i}[n]$, as detailed in (7) and (8).

$$p_{x,i}[n] = \frac{\max(r_i[n])}{\max(s_i[n])} \tag{7}$$

$$p_{y,i}[n] = \frac{\max(t_i[n])}{\max(s_i[n])} \tag{8}$$

Where $s_i[n]$, $t_i[n]$, and $r_i[n]$ are the correlations between the received signals $V_{sum}[n]$, $V_{BT}[n]$ and $V_{LR}[n]$ and the corresponding sequence $c_i[n]$ for every LED $i$, respectively.

Fig. 6 shows an example of the theoretical above-mentioned correlations at a particular point of the space for LEDs $i$={1,2,3,4}. It can be observed how the correlations differ from one transmitter $i$ to another depending on the transmitter location. Those LEDs located at further distances from the receiver provide worse correlation functions (see, for instance, Fig. 6.b for LED $i$ = 3). That means that the maximum peak may not be clearly detected. In order to minimize that possibility, in the proposed algorithm, maximum peaks are initially selected in the correlation function $s_i[n]$, since this function always present higher amplitudes than the others, thus making the correlation peaks easier to be identified. Afterwards, the other correlation peaks in functions $r_i[n]$ and $t_i[n]$ are located, just by taking into account where they should be accordingly to the displacements of the transmissions carried out previously. Therefore, this method of determining the correlation peaks provides the system with a significant robustness against very low signal to noise ratios, and multipath and near-far effects.

### *B. Central Impact point estimation*

The position ($x_r$, $y_r$), where light passing through the center of the aperture impacts, is estimated by *Non-Linear Least Squares (NLS)* using the *Gauss-Newton* algorithm. Before applying NLS, two tables with theoretical predefined ratios $p_x$ and $p_y$ are characterized for the plane where the receiver is placed, in a range [-$r$, $r$] at intervals of 1 µm, thus performing a geometrical characterization of the receiver's areas as detailed in the Appendix A. (note that $r$ = 3.9 mm). It is worth noting that this geometrical characterization does not involve certain approximations as in [22], taking into account an accurate round shape of the QADA receiver instead. In addition, these tables can be calibrated to consider practical deviations of some intrinsic parameters of the receiver (e.g. aperture height).

As can be observed in Fig. 7.a) where $p_x$ is represented, there is a wide range around the centre of the QADA receiver where the values for $p_x$ are hard to be directly extracted from the graph, since they are extremely similar for different $y_r$ values (low derivative).

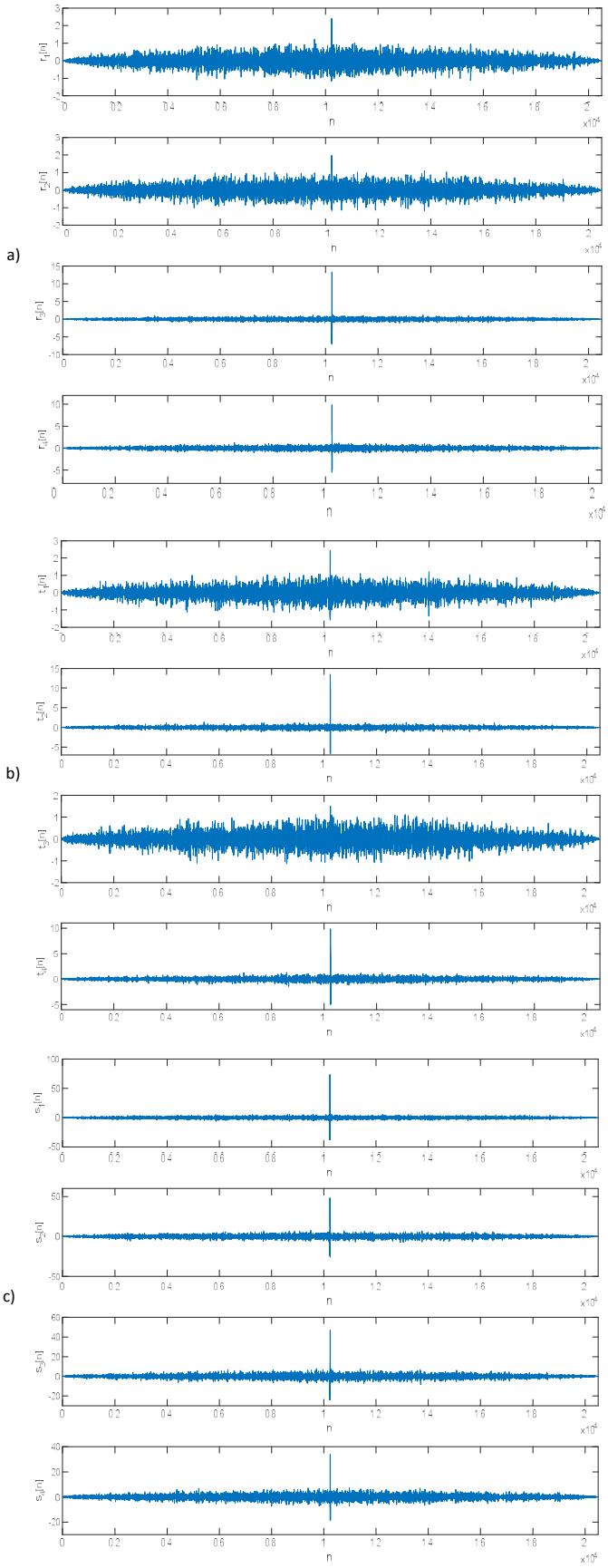


Fig. 6. Example of the correlation functions computed at the reception: a) $r_i[n]$; b) $t_i[n]$; and c) $s_i[n]$.

To avoid this lack of sensitivity, these aforementioned ratio tables are actually calculated as the square root of the absolute value of the ratios $p_x$ and $p_y$, still considering the sign of the ratios $p_x$ and $p_y$, respectively, as can be observed in Fig. 7.b) for the case of $p_x$. As a result, a greater slope in the centre of the QADA ($x_r$=0, $y_r$ = 0) (see zoomed plots in Fig. 7) is obtained. It is worth noting that only those ratio tables related to the ratio $p_x$, depending on $x_r$ for all the ranges in $y_r$ (3), are plotted in Fig. 7. Similarly, tables about ratio $p_y$ provide similar information.

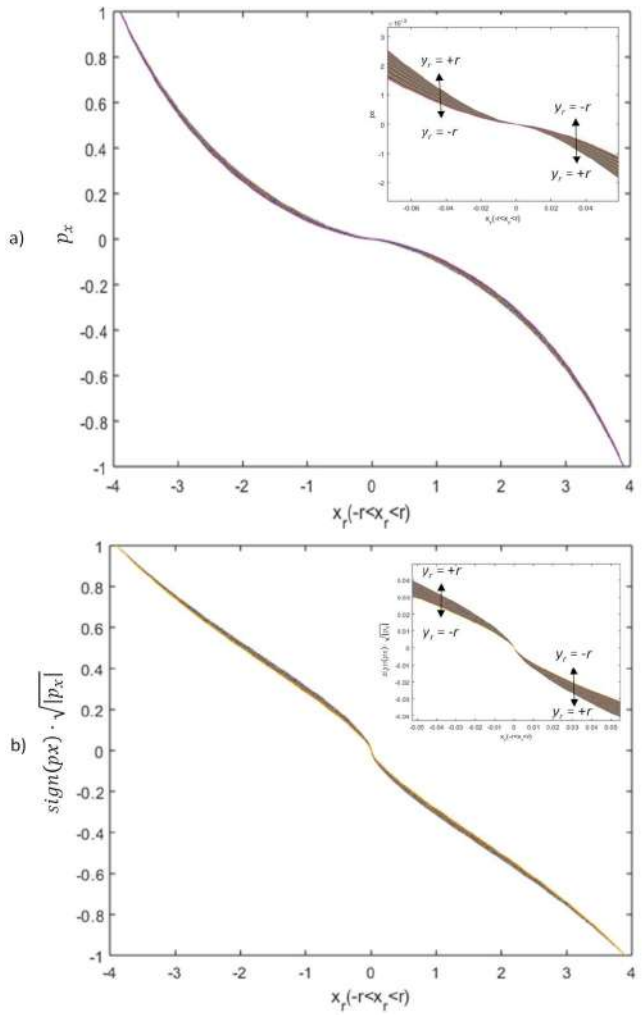


Fig. 7. Ratio $p_x$ depending on the coordinate $x_r$ for a range of values in $y_r$; $x_r \in [-r, r]$, $y_r \in [-r, r]$ a) Ratio $p_x$; b) Square root of the absolute value of the ratio $p_x$, still considering the sign of $p_x$: $sign(p_x)\cdot\sqrt{|p_x|}$.

The algorithm involved in the calculation of the position ($x_r$, $y_r$) starts with the initialization of a threshold $u$, which is actually the maximum error allowed by the iterative algorithm; in this case, it is fixed at $u$ = 1µm. While the threshold $u$ is lower than the detected errors $\varepsilon_{s,1}$ for $x_r$ and $\varepsilon_{s,2}$ for $y_r$ at a certain iteration $s$, the algorithm will continue iterating. A predefined Jacobian matrix is obtained in (9), by means of the above-mentioned tables, according to ($x_r$, $y_r$).

$$\mathbf{J} = \begin{bmatrix} \frac{\delta p_x}{\delta x_r} & \frac{\delta p_x}{\delta y_r} \\ \frac{\delta p_y}{\delta x_r} & \frac{\delta p_y}{\delta y_r} \end{bmatrix} \tag{9}$$

Where the finite derivatives $\frac{\delta p_x}{\delta x_r}, \frac{\delta p_x}{\delta y_r}, \frac{\delta p_y}{\delta x_r}$ and $\frac{\delta p_y}{\delta y_r}$ are calculated as an approximation of the first-order derivative (10-13). Note that the constant $n$ is considered to be 1 µm, which is the step between intervals considered in the tables for ratios $p_x$ and $p_y$.

$$\frac{\delta p_x}{\delta x_r} = \frac{4\cdot p_x(x_r+n) - 3\cdot p_x(x_r) - p_x(x_r+2\cdot n)}{2\cdot n} \tag{10}$$

$$\frac{\delta p_x}{\delta y_r} = \frac{4\cdot p_x(y_r+n) - 3\cdot p_x(y_r) - p_x(y_r+2\cdot n)}{2\cdot n} \tag{11}$$

$$\frac{\delta p_y}{\delta x_r} = \frac{4\cdot p_y(x_r+n) - 3\cdot p_y(x_r) - p_y(x_r+2\cdot n)}{2\cdot n} \tag{12}$$

$$\frac{\delta p_y}{\delta y_r} = \frac{4\cdot p_y(y_r+n) - 3\cdot p_y(y_r) - p_y(y_r+2\cdot n)}{2\cdot n} \tag{13}$$

The algorithm starts by searching for the values of an initial position $(x_r, y_r)_0$ into the ratio tables, and the corresponding errors $\varepsilon_{s,1}$ and $\varepsilon_{s,2}$ are calculated (14).

$$\begin{bmatrix} \varepsilon_1 \\ \varepsilon_2 \end{bmatrix}_s = \begin{bmatrix} p_x \\ p_y \end{bmatrix} - \begin{bmatrix} p_x \\ p_y \end{bmatrix}_s \tag{14}$$

Where $p_x$ and $p_y$ are the measured values from the correlation peaks (7) and (8); and $p_{x,s}$ and $p_{y,s}$ are the values obtained from the search in the ratio tables for the desired predefined values of the ratios $p_x$ and $p_y$ for the position $(x_r, y_r)_s$. After the errors $\varepsilon_{s,1}$ and $\varepsilon_{s,2}$ are calculated, the previous solution $(x_r, y_r)_s$ is updated (15) for the next iteration $(x_r, y_r)_{s+1}$.

$$\begin{bmatrix} x_r \\ y_r \end{bmatrix}_{s+1} = \begin{bmatrix} x_r \\ y_r \end{bmatrix}_s + \left( \mathbf{J}^T_{\begin{bmatrix} x_r \\ y_r \end{bmatrix}_s} \cdot \mathbf{J}_{\begin{bmatrix} x_r \\ y_r \end{bmatrix}_s} \right)^{-1} \cdot \mathbf{J}^T_{\begin{bmatrix} x_r \\ y_r \end{bmatrix}_s} \cdot \begin{bmatrix} \varepsilon_1 \\ \varepsilon_2 \end{bmatrix}_s \tag{15}$$

Where $\mathbf{J}_{\begin{bmatrix} x_r \\ y_r \end{bmatrix}_s}$ is the Jacobian matrix **J** for the current estimated position $(x_r, y_r)_s$; and $\mathbf{J}^T_{\begin{bmatrix} x_r \\ y_r \end{bmatrix}_s}$ is the transposed of the Jacobian matrix **J** for the current estimated position $(x_r, y_r)_s$. The new position $(x_r, y_r)_{s+1}$ will enter again in the NLS algorithm until the convergence of the algorithm, when the error is lower than the threshold, i. e. $\sqrt{x_r^2 + y_r^2}_s < u$. It is worth mentioning that the iterative algorithm stops when that convergence criteria is met [49].

Furthermore, the procedure have been modified to avoid any out-of-range result, so the column and/or row indexed by the position $(x_r, y_r)_s$ in the ratio tables always remains inside their dimensions. Whether the algorithm searches for a column/row outside the dimensions of the ratio tables, it will be readdressed to a column/row contained in the table. Note that, although it is an infrequent event, it may occur when the point of incidence is near the border of the QADA receiver.

For a better understanding of the aforementioned NLS algorithm, a flowchart is presented in Fig. 8. The iterative cycle starts at $(x_r, y_r)_s$, whereas the transpose is indicated by the block T and the inverse is denoted as $(\,)^{-1}$.

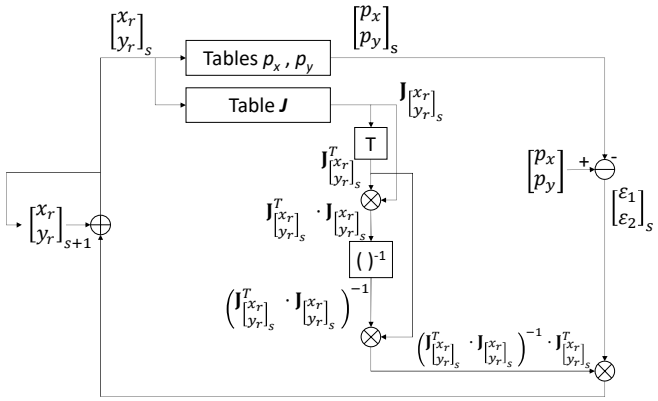


Fig. 8. Flowchart of the proposed NLS algorithm.

## IV. Positioning Algorithm

For the sake of clarity, it is assumed that three or more impact points $(x_r, y_r)_i$ are known, as well as the locations of their corresponding transmitters $i$, so the receiver can estimate its own location by means of the *Least Squares Estimator* (LSE) [50]. In this case, when considering the scenario proposed in Fig. 9, the point $(x, y)$ is the 2D position of the receiver, $(x_{t,i}, y_{t,i})$ are the positions for every LED $i$, and $\gamma_i$ are the angles between the transmitters $i$ and the $X$ axis. Thus, note that the positioning algorithm is actually based on triangulation techniques.

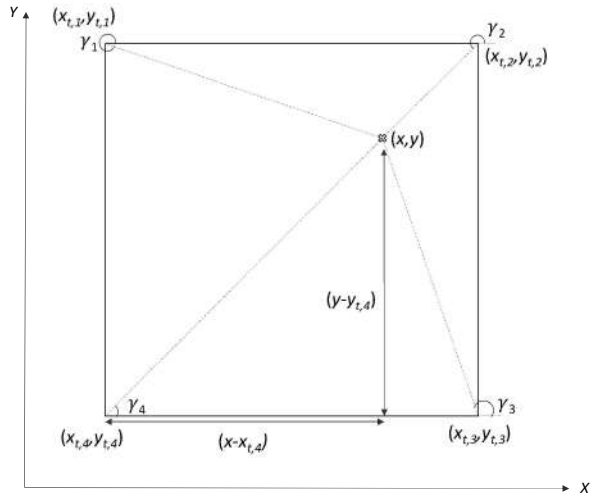


Fig. 9. 2D geometrical analysis of the proposed system.

From Fig. 9, the geometrical expression (16) can be written as (17).

$$\tan(\gamma_i) = \frac{\sin(\gamma_i)}{\cos(\gamma_i)} = \frac{\Delta y}{\Delta x} = \frac{y - y_{t,i}}{x - x_{t,i}} \tag{16}$$

$$-\mathrm{x} \cdot \sin(\gamma_i) + x_{t,i} \cdot \sin(\gamma_i) = -y \cdot \cos(\gamma_i) + y_{t,i} \cdot \cos(\gamma_i) \tag{17}$$

Keeping in mind the geometrical distribution of the QADA receiver and its aperture shape in Fig. 10, it is possible to obtain (18), similarly to (16). Since the receiver is neither rotated nor tilted, then $\gamma_i = \theta_i$, so Eq. (17) can be simplified according to (19).

$$\tan(\theta_i) = \frac{\sin(\theta_i)}{\cos(\theta_i)} = \frac{y_{r,i}}{x_{r,i}} \tag{18}$$

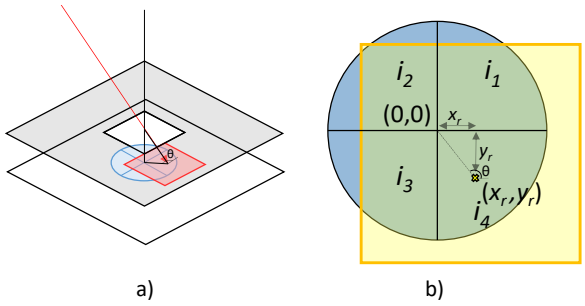


Fig. 10. a) Incident light in the photoreceiver; b) Geometrical analysis of the receiver.

$$-\mathrm{x} \cdot y_{r,i} + x_{t,i} \cdot y_{r,i} = -y \cdot x_{r,i} + y_{t,i} \cdot x_{r,i} \tag{19}$$

Eq. (19) can be transformed into a matrix form $\boldsymbol{A} \cdot \boldsymbol{X} = \boldsymbol{b}$, where the least squares method estimates the global coordinates $(x, y)$ of the receiver (20).

$$(x, y) = (\boldsymbol{A}^T \cdot \boldsymbol{A})^{-1} \cdot \boldsymbol{A}^T \cdot \boldsymbol{b} \tag{20}$$

Where $\boldsymbol{A} = \begin{bmatrix} -y_{r,1} & x_{r,1} \\ -y_{r,2} & x_{r,2} \\ -y_{r,3} & x_{r,3} \\ -y_{r,4} & x_{r,4} \end{bmatrix}$ and $\boldsymbol{b} = \begin{bmatrix} y_{t,1} \cdot x_{r,1} - x_{t,1} \cdot y_{r,1} \\ y_{t,2} \cdot x_{r,2} - x_{t,2} \cdot y_{r,2} \\ y_{t,3} \cdot x_{r,3} - x_{t,3} \cdot y_{r,3} \\ y_{t,4} \cdot x_{r,4} - x_{t,4} \cdot y_{r,4} \end{bmatrix}$.

After estimating the location $(x, y)$ of the receiver in 2D, the third dimension $z$ is obtained by means of the triangulation relationship detailed in Fig. 11, where the incident angle $\Psi$ was already defined in Section III (see Fig. 2) (2), and $d_i$ is the distance between the estimated receiver's position $(x, y)$ and the projection of each transmitter $i$ in the plane where the receiver is placed. Thus, the coordinate $z$ is obtained as the averaged value from the differences between the height $z_{t,i}$ of the transmitters $i$ and the geometrically calculated height $h_i$ (21-22).

$$h_i = \frac{d_i}{tan(\psi_i)} \tag{21}$$

$$z = \frac{\sum_{i=1}^{4}(z_{t,i} - h_i)}{4} \tag{22}$$

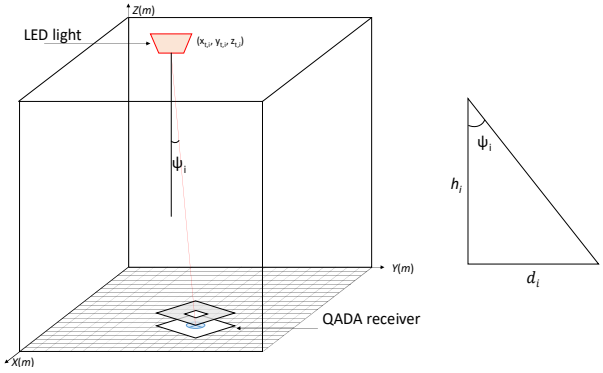


Fig. 11. Scenario of the positioning analysis for the distance $h_i$ between a transmitter $i$ and the receiver. Note that elements are not to scale.

### A. Computational Load of the Positioning Algorithm

The computational load of the proposed positioning algorithm has been evaluated in Table II, where $M$ is still the oversampling factor; $L$ is the length of the Kasami sequences $c_i$ involved; $I$ is the number of LEDs; and $N$ is the number of iterations performed in the NLS algorithm. In this proposal, the parameters mentioned above are, typically, $M$ = 10, $L$ = 1023, $I$=4 and $N$ = 5. As can be observed, the complexity of the proposed algorithm mainly relies on the number $I$ of LEDs. In a more detailed way, the operations required for the sequence correlations are only additions, proportional to $M$, $L$ and $I$; the NLS algorithm implies both multiplications and additions, depending on $N$ and $I$; the LSE algorithm requires $O(I^2)$ for both; and the ratios calculation and the estimation of coordinate $z$ involve division, proportional to $I$. It is worth noting that the Jacobian matrix and its corresponding operations in the Gauss-Newton algorithm are considered to be previously calculated and preloaded, so they do not imply any burden for the algorithm's computational complexity.

On the other hand, with regard to the power consumption, it will mainly depend on the final platform used for the implementation of the proposal.

TABLE II
NUMBER OF OPERATIONS FOR EVERY TASK IN THE PROPOSED POSITIONING ALGORITHM.

| Task | Addition | Multiplication | Division |
|---|---|---|---|
| **Correlation** | $3(M{\cdot}L\text{-}1){\cdot}I$ | - | - |
| **Ratios calculation** | - | - | $2{\cdot}I$ |
| **NLS** | $6{\cdot}N{\cdot}I$ | $4{\cdot}N{\cdot}I$ | - |
| **LSE** | $I^2{+}3{\cdot}I\text{-}1$ | $I^2{+}6{\cdot}I{+}2$ | $I$ |
| **Estimation of coordinate z** | $2{\cdot}I\text{-}1$ | - | $I$ |

### B. Simulated Results

Hereinafter, the positioning method proposed in this work has been particularized for certain parameters. The dimensions of the room to be analysed are 2 x 2 x 2 m$^3$ with four LEDs installed at 2 m high (see Fig. 1). For simplicity, the LED lamps are modelled as a point source (see Table I). The rest of the simulation parameters are detailed in Table III. In addition to the parameters described before, a Gaussian Noise has been added in the received signal in order to have a signal-to-noise ratio (SNR) of 10 dB. Simulations were carried out a hundred times at every position for all the X-Y positions in a grid (with a step of 10 cm), and at different planes $z$ = 0 m, 0.5 m, 1 m, 1.5m.

TABLE III
DESIGN PARAMETERS USED IN THIS STUDY

| Parameter | Value |
|---|---|
| Aperture height $h_{ap}$ | 2.6 mm |
| QADA radius | 3.9 mm |
| Volume under analysis | 2 x 2 x 2 m$^3$ |
| Transmitters beam angle | 120º |
| SNR | 10 dB |

Fig. 12 details the absolute errors of the incident angle $\Psi$ depending on the ($x$, $y$) position, for a particular LED $i$. A cross represents the position of this LED $i$ on the plane. It can be verified that those positions with the larger absolute errors appear around the transmitter's position for $z$ = 0 m, 0.5 m and 1 m. In the case of $z$ = 1.5 m, the receiver is actually too close to the transmitter $i$, so the error is generalized all around the area. Accodingly, the performance degrades as the height $z$, where the receiver is located, increases for all the incident angles $\Psi$.

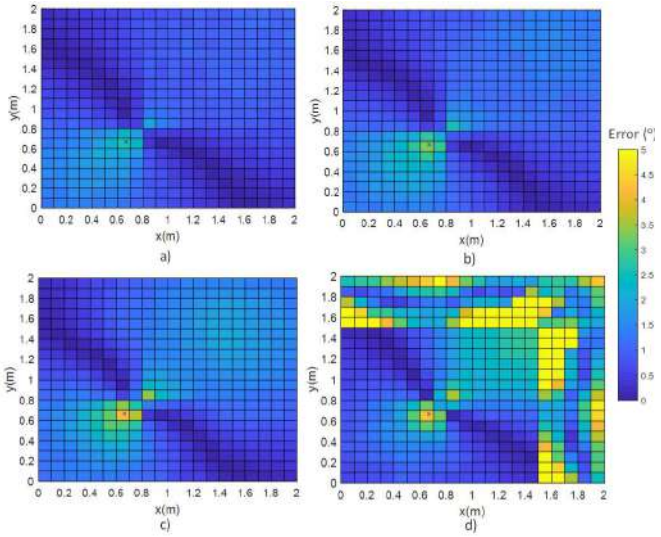


Fig. 12. Absolute error of the incident angle $\Psi$ for transmitter $i$ = 4 at: a) $z$=0m; b) $z$ = 0.5 m; c) $z$ = 1 m; d) $z$ = 1.5 m.

The projection of the errors analysed in Fig. 12.a) for $z$ = 0 m has been extended to the four proposed transmitters (see their positions in Table I), as can be observed in Fig. 13. This allows to confirm that, due to the symmetry of the system, the results obtained here with a single transmitter can be easily extended to all the transmitters $i$ = {1,2,3,4}.

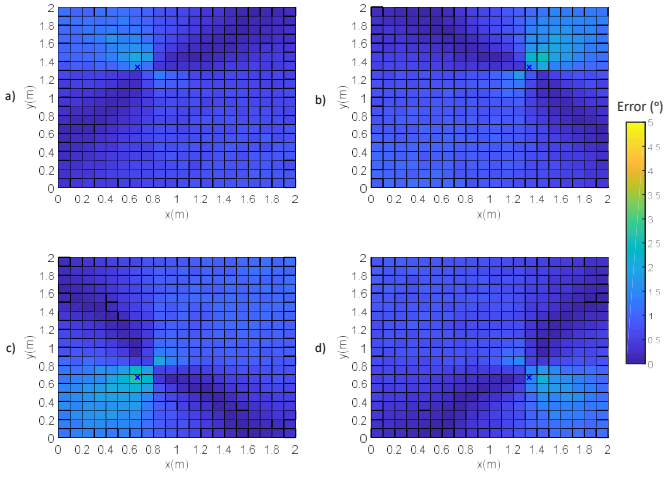


Fig. 13. Absolute error of the incident angle $\Psi$ at $z$ = 0 m for transmitters: a) LED $i$ = 1; b) LED $i$ = 2; c) LED $i$ = 4; d) LED $i$ = 3.

As was already detailed in Fig. 4 and Fig. 12, at plane $z$=1.5m relevant errors emerge due to the proximity between the transmitters and the receiver. Therefore, Fig. 14 plots the cumulative distribution function (CDF) for the absolute error of

the incident angle $\Psi$ in a 2 x 2 m$^2$ grid, in steps of 0.10 m, at different planes $z$ = 0 m, 0.5 m, 1 m for only one transmitter $i$, then discarding $z$ = 1.5 m hereinafter. A hundred of iterations has been run at each of those points within the volume of coverage detailed in Fig. 4. A minimum absolute error of 1.4º is achieved in the 90% of the cases at $z$ = 0 m.

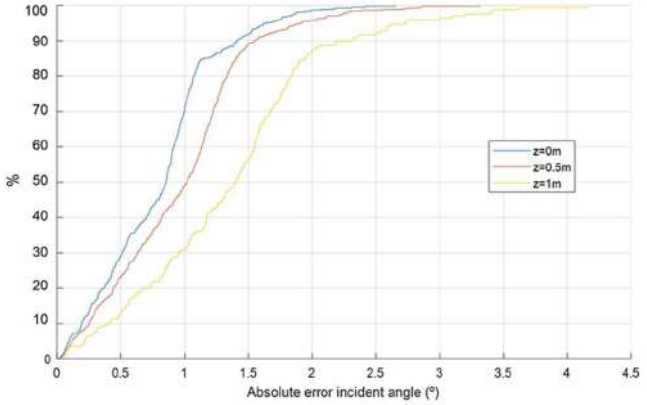


Fig. 14. CDF of the absolute error in the determination of the incident angle $\Psi$ at LED $i$ at $z$ = 0 m, 0.5 m, 1 m.

The projection of the absolute errors of the receiver's estimated position $(x, y)$ is presented in Fig. 15, Fig. 16 and Fig. 17 for coordinates $x$, $y$ and $z$ respectively, at planes $z$ = 0 m, 0.5m and 1 m (black crosses represent the projections of the position of the LEDs $i$ on the corresponding plane).

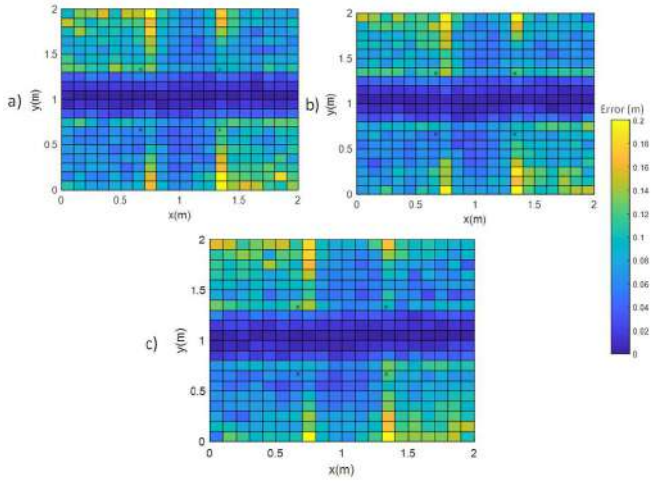


Fig. 15. Absolute errors for coordinate $x$ at: a) $z$ = 0 m; b) $z$ = 0.5 m; c) $z$=1m.

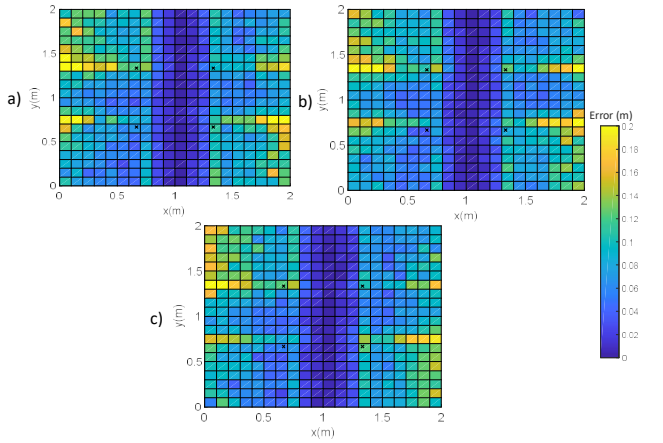


Fig. 16. Absolute errors for coordinate $y$ at: a) $z$ = 0 m; b) $z$ = 0.5 m; c) $z$ = 1 m.

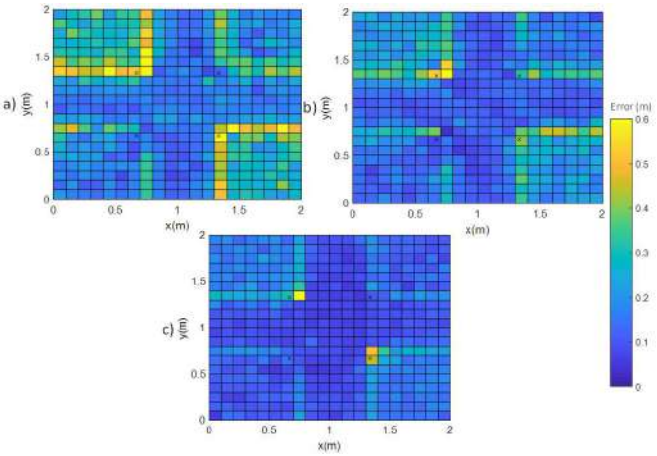


Fig. 17. Absolute errors for coordinate $z$ at: a) $z$ = 0 m; b) $z$ = 0.5 m; c) $z$ = 1 m.

Those positions with the largest absolute errors appear in line with the transmitters' coordinate $x$ for the absolute error of the coordinate $x$ (see Fig. 15), and in line with the transmitters' coordinate $y$ for the absolute errors of the coordinate $y$ (see Fig. 16), for $z$ = 0 m, 0.5 m and 1 m. This dependence of the errors in the receiver's position with respect to the transmitters' positions was already presented in (20), since, whether both coordinate values ($x_{t,i}$ and $x_{r,i}$, or $y_{t,i}$ and $y_{r,i}$) are nearly equal, an indetermination appears. On the other hand, errors for coordinate $z$ are mainly due to the accumulation of errors from coordinates $x$ and $y$ in the estimation of the distance $d_i$ (21-22).

Furthermore, in Fig. 18, the CDF for the absolute errors of the estimated position $(x, y)$ of the receiver is shown at different planes $z$ = 0 m, 0.5 m, 1 m, just considering the actual coverage area at each plane (see Fig. 4). As before, for every plane a hundred of iterations has been run at each of the points in a 2x2m$^2$ grid, with steps of 0.10 m.

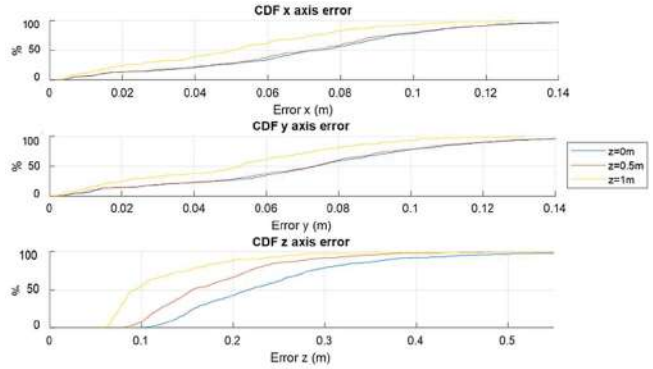


Fig. 18. CDF for the absolute error of the positioning error in the receiver's coordinates $(x, y, z)$ at $z$ = 0 m, 0.5 m, 1 m.

Absolute errors in the range of 10 - 11 cm are provided whether the receiver is placed at $z$ = 0 m, 0.5 m, for both $X$ and $Y$ axes in the 90% of the considered cases. Besides, the absolute errors obtained at $z$ = 1 m are in the range of 7 – 8 cm, much lower than those at $z$ = 0 m and 0.5 m. This is due to the fact that the coverage area analysed here is significantly smaller, as a consequence of a shorter distance between the receiver and the transmitters $i$.

For further comparisons, the receiver has been placed at nine known positions in the coverage area, where a hundred of

simulations has been run at every position, with a SNR = 10 dB and assuming Gaussian noise. These nine positions will be further considered in the experimental results and have been selected to cover mostly the half right side of the coverage area, since similar results are expected on the left side (if the symmetries of the arrangement are considered). Fig. 19 plots these simulation results, where the red crosses are the real measurement point (ground-truth); the black crosses represent the projection of the LED lamps $i$; and, the coloured point clouds are the obtained position estimates in the simulation. An error ellipsoid is also plotted with a 95% of confidence for every measurement point. It is possible to observe that there is no large dispersion in the obtained results, apart from the corner points. Also, it is worth noting that the obtained average errors are 7 cm and 5 cm for measured points in the $X$ and $Y$ axes at planes $z$ = 0 m and $z$ = 1 m, respectively. In particular, the average of the $X$ axis error in the measured points is 3.6 cm for $z$ = 1 m and 4 cm for $z$ = 0 m; the $Y$ axis has an average error of 4.9 cm for $z$ = 1 m and 5.1 cm for $z$ = 0 m; and the $Z$ axis average errors are 12.5 cm for $z$ = 1 m and 19.1 cm for $z$ = 0 m.

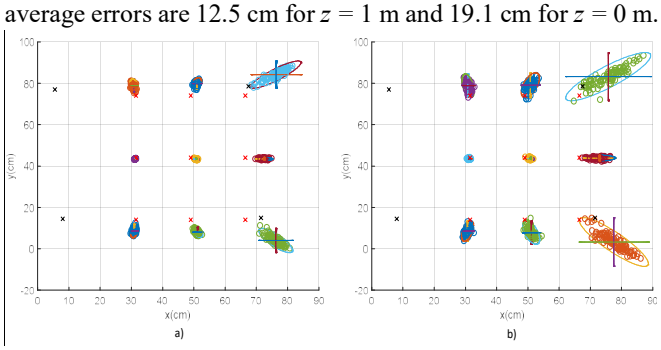


Fig. 19. a) Simulated position estimates when the receiver is placed at $z$ = 1 m; b) Simulated position estimates when the receiver is placed at $z$ = 0 m.

It is worth mentioning that the existing systematic error in the position estimates, which can be observed in Fig. 19, is caused by a multiple-access interference (MAI), coming from the simultaneous transmissions by the LEDs, whose cross correlations interfere in the positioning algorithm. This issue can be easily tackled by separating completely the corresponding emissions, so any MAI effect can be discarded. The cost is a longer time to determine the position because emissions are consecutive and not simultaneous. This case is depicted in Fig. 20 at $z$ = 0 m for coordinates $x$ and $y$ without considering any noise. As can be observed, errors in the range of $10^{-4}$ are present in the whole area, which are much lower than those obtained in Figs. 15.a) and 16.a), thus verifying no systematic errors appear when there is no MAI.

## V. Experimental Results

The experimental setup implemented here involves four LED lamps located at plane $z$ = 2 m and the QADA receiver, which is placed at planes $z$ = 0 m and $z$ = 1 m. Fig. 21 shows this setup when the receiver is placed at $z$ = 0 m. As can be observed in Figs. 21 and 22, others lamps in the room were also turned on during experiments. This particular ambient light, as well as the incoming sunlight from the windows, are considered to be equal in all the receiver surface and, thus, it will be eliminated by means of the correlation functions computed with the transmitted codes $c_i$. Therefore, no variations due to this noise will affect the algorithm previously described.

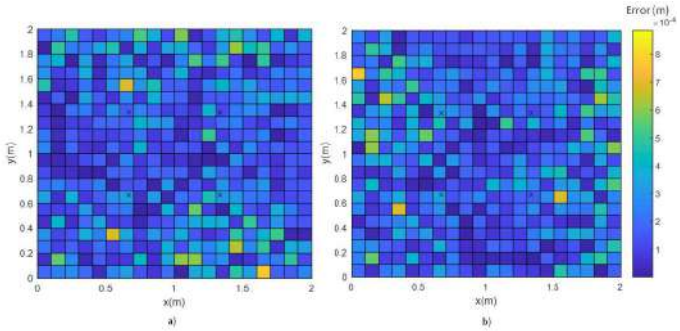


Fig. 20. Absolute errors with fully separated transmissions at $z$ = 0 m for coordinates: a) $x$ and b) $y$.

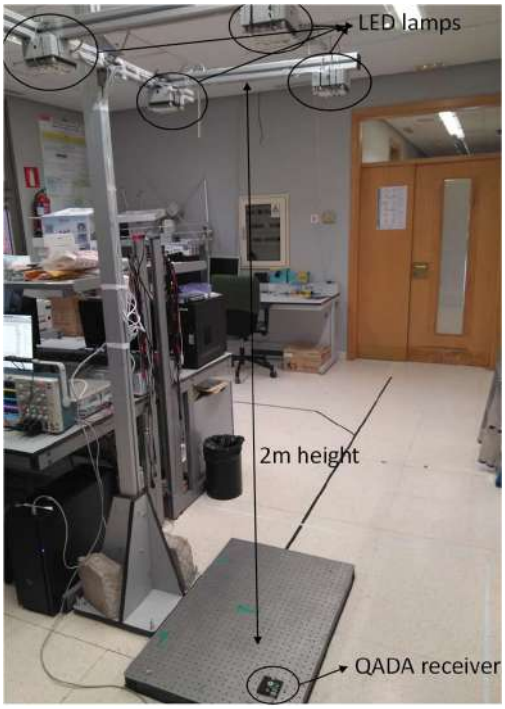


Fig. 21. Experimental setup implemented for the proposal validation.

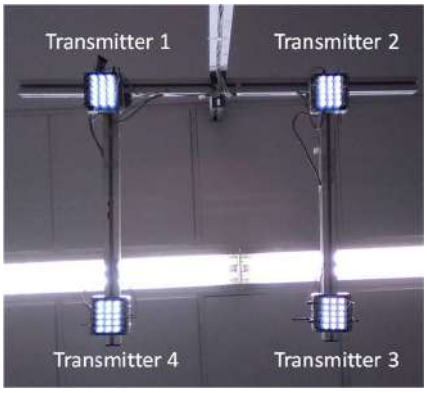


Fig. 22. Detail of LED lamps during transmission.

The area under analysis is the same as the previous one detailed in Section IV. The receiver has been placed at each one of the same nine points considered before, and the corresponding positions have been obtained up to 50 times per point. Fig. 23 plots these experimental results, where the red crosses are the ground-truth again; the black crosses represent the projection of the LED lamps *i*; and, the coloured point clouds are the positions obtained for the receiver. An error ellipse is also plotted with a 95% of confidence for each one of the nine measured points in the plane *XY*.

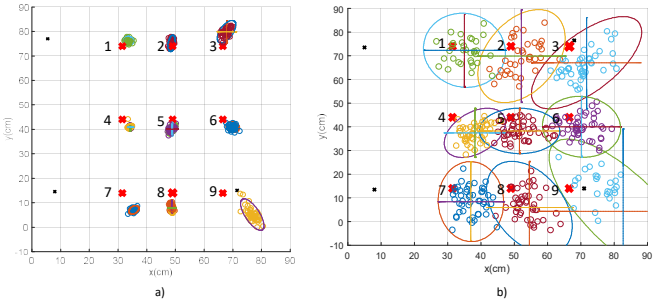


Fig. 23. a) Experimental position estimates when the receiver is placed at $z$=1m; b) Experimental position estimates when the receiver is placed at $z$ = 0 m.

Accordingly, those measurements obtained at $z$ = 1 m match those expected from simulation in Fig. 19. It is worth noting that these average errors are below 5 cm for all the measured points in the *X* and *Y* axes, except for points 3 and 9 where the dispersion is slightly higher. Note that the results obtained at $z$ = 0 m do not match those expected from Fig. 19, since the SNR = 10 dB used in Fig. 19 describes a better scenario than the one found in the experimental results. Note that higher distances imply lower SNR. Then, a higher emitting power from the transmitters *i*, as well as the consideration of the real dimensions of transmitters instead of point-like, may decrease the dispersion in Fig. 23.b), with results more similar to those expected from simulations. The effect of not point-like light sources has already been analysed in [25], where it is concluded that increasing the size of the LED lamps largely increases the positioning error in the limits of the analysed scenario. In Fig. 24 the position estimation simulated in Fig. 19.b) is repeated with SNR = 3 dB, thus matching results in Fig. 23.b).

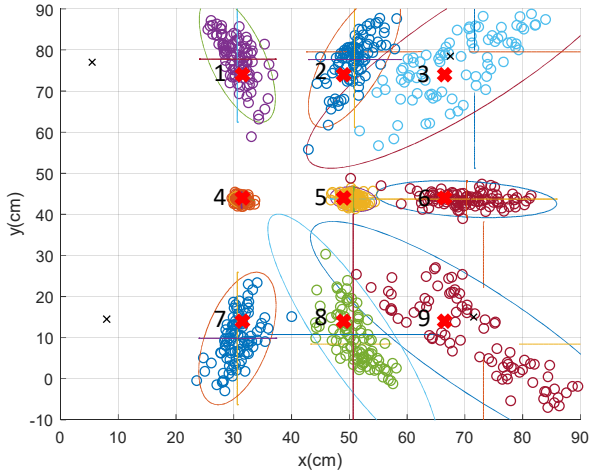


Fig. 24. Simulated position estimates when the receiver is placed at z = 0 m with SNR = 3 dB.

The average absolute error and the average standard deviation obtained in the experimental position are estimated for the nine considered points as detailed in Table IV, whereas the same parameters are detailed for the simulation results in Table V, both providing similar figures. Note that in Table V the results presented in $z$ = 0, 1 m are those from Fig. 24 (SNR=3dB) and Fig. 19 (SNR = 10dB), respectively.

TABLE IV
AVERAGE ABSOLUTE ERRORS AND STANDARD DEVIATIONS FOR THE NINE POINTS CONSIDERED IN THE EXPERIMENTAL RESULTS FROM FIG. 23.

| Axis | $z$ = 1 m | | $z$ = 0 m | |
|---|---|---|---|---|
| | Average absolute error | Average standard deviation | Average absolute error | Average standard deviation |
| *X* axis | 2.8 cm | 0.78 cm | 6.43 cm | 4.88 cm |
| *Y* axis | 4.62 cm | 1.14 cm | 7.28 cm | 6.31 cm |
| *Z* axis | 5.57 cm | 2.5 cm | 24.16 cm | 18.77 cm |

TABLE V
AVERAGE ABSOLUTE ERRORS AND STANDARD DEVIATIONS FOR THE NINE POINTS CONSIDERED IN THE SIMULATION RESULTS FROM FIG. 19 AND FIG. 24.

| Axis | $z$ = 1 m | | $z$ = 0 m | |
|---|---|---|---|---|
| | Average absolute error | Average standard deviation | Average absolute error | Average standard deviation |
| *X* axis | 3.64 cm | 0.88 cm | 4.46 cm | 4.73 cm |
| *Y* axis | 4.89 cm | 1.02 cm | 5.36 cm | 5.76 cm |
| *Z* axis | 12.51 cm | 4.72 cm | 25.9 cm | 30.82 cm |

In addition, Table VI presents a comparison among some previous works focused on VLPS. These works implement different multiplexing techniques: Frequency Division Multiple Access (FDMA) [51], Code Division Multiple Access (CDMA) [20], Time Division Multiple Access (TDMA) [52], and Orthogonal Frequency Division Multiplexing (OFDM) [53] [55]; to use their bandwidth and develop Visible Light Communication (VLC) links. It may be remarked that some works involve other sensors, such as mechanical ones (IMU) [31] [53] or accelerometers [52], to increase their area of operation while decreasing the positioning error. In addition, Avalanche Photodiodes (APD) are used in [54] to increase the receiver sensitivity. On the other hand, among those using several photodetectors (PD) [52] - [56], the solution proposed here reaches the lowest errors with the less hardware involved at the receiver. In [31] [53] [55] the proposal is tested in a large area of operation, thus resulting in significant positioning errors. Summing it up, the proposal presented here provides a good average positioning error, similar to [20] and [56]; although in these works the tests were performed at a maximum distance of 1.1 m and 0.5 m, respectively, between the emitters' plane and the receiver's one (up to 2 m in our case). Furthermore, note that [56] implies a more complex receiver (it is actually an array of sensors).

TABLE VI
COMPARISON WITH PREVIOUS POSITIONING SYSTEMS BASED ON VISIBLE LIGHT

| | | Number of beacons | Power of each beacon | Modulation/ Codification | Distance between transmitter and receiver | Type of receiver | Area of operation | Position accuracy | Positioning technique |
|---|---|---|---|---|---|---|---|---|---|
| [51] | 2D | 4 | | FDMA, PWM | 1.2 m | 1 PD | 3 x 3 $m^2$ | <10 cm (CDF 95) | RSS |
| [20] | 3D | 4 | 9 W | CDMA | 1.1 / 0.7 /0.3 m | 1 PIN | 0.9 x 0.9 $m^2$ | 4 cm (average) | RSS |
| [31] | 2D | 7 | 17 W | OOK | 2.5 m | 1 PD + IMU | 2.2 x 2.2 $m^2$ | 14.5 cm (average) | RSS + PDR |
| [52] | 3D | 3 | | TDMA | 1.7 m | 4 PDs + accelerometer | 0.4 x 0.4 $m^2$ | <10 cm<br>6 cm (average) | RSS |
| [53] | 3D | 4 | 1.5 W | OFDM | 1 / 0.42 m | 9 PD with apertures + IMU | 5 x 5 $m^2$ | 18 / 8.6 cm (average) | AoA |
| [54] | 3D | 3 | 1 W | - | 1.5 m | 2 APD + reference detector | 1 x 1 $m^2$ | < 10 cm (average) | RSS |
| [55] | 3D | 4 | 1 W | OFDM | 2 m | 8 PDs with apertures | 5 x 5 $m^2$ | < 20 cm (rMSE) | AoA |
| [56] | 3D | 4 | 57 mW | - | 0.5 m | 3 PD arranged in a corner-cube structure | 0.3 x 0.3 $m^2$ | 5 cm ( average) | AoA |
| Proposal | 3D | 4 | 7.5 W | BPSK,CDMA | 2 / 1 m | 1 QADA with aperture | 2 x 2 $m^2$ (simulations)<br>0.7 x 0.7 $m^2$ (experimentation) | 12 / 8 cm (CDF 95)<br>7.42 / 3.96 cm (2D average)<br>13 / 5.5 cm (3D average) | AoA |

## VI. CONCLUSION

This work presents a study of a three-dimension visible light indoor positioning system (VLPS), based on four LED lamps as transmitters and a quadrant photodiode as receiver. An encoding scheme based on 1023-bit Kasami sequences has been applied to every transmission coming from each LED lamp that can be identified by the receiver, thus providing multiple access capability and a significant improvement of the system to deal with low signal-to-noise ratios, and different types of hindering phenomena, such as multipath and near-far effect. The corresponding correlation functions have been used to estimate the central incidence points from each LED on the quadrant receiver, by using Non-Linear Least Squares (NLS) with a Gauss-Newton algorithm. A triangulation technique, solved by LSE and some geometrical considerations, has been proposed to estimate the receiver's position inside the corresponding coverage area. The proposal has been evaluated and successfully verified by means of simulations and experimental results, achieving both a significant concordance, with 3D positioning average errors below 13 cm and 5.5 cm when the separation in height between the emitters and the receiver is 2 m and 1 m, respectively.

## APPENDIX

### A. Estimation of the QADA areas

The purpose of this appendix is to present a detailed calculation of the different areas $A_j(t)$ for $p_x(t)$ (3) in the first quadrant, $x_r, y_r \in [0, r]$ (23-27), where $r$ = 3.9 mm is the radius of the photoreceiver QADA. Similarly, this study can be extended to the other quadrants and, also, to perform the analysis for $p_y(t)$. Note that the third quadrant has an area $A_3(t)$ that depends on the position at which the projection of the aperture is located in the photoreceptor, as is shown in Fig. 25 and is detailed in (25) and (26) for the two cases $A_{3,1}(t)$ and $A_{3,2}(t)$, respectively.

$$A_1(t) = \frac{\pi \cdot r^2}{4} \tag{23}$$

$$A_2(t) = \frac{\pi \cdot r^2}{4} - \frac{1}{2} \cdot \left[\frac{r^2}{2} \cdot (\theta - \sin(\theta))\right] \tag{24}$$

$$A_{3,1}(t) = (r - x_r) \cdot (r - y_r) \tag{25}$$

$$A_{3,2}(t) = \frac{\pi \cdot r^2}{4} - \frac{1}{2} \cdot \left[\frac{r^2}{2} \cdot (\theta - \sin(\theta))\right] - \frac{1}{2} \cdot \left[\frac{r^2}{2} \cdot (\theta' - \sin(\theta'))\right] \tag{26}$$

$$A_4(t) = \frac{\pi \cdot r^2}{4} - \frac{1}{2} \cdot \left[\frac{r^2}{2} \cdot (\theta' - \sin(\theta'))\right] \tag{27}$$

Where $r$ is the radius of the receiver; and $\theta = 2 \cdot \text{acos}\left(1 - \frac{x_r}{r}\right)$ and $\theta' = 2 \cdot \text{acos}\left(1 - \frac{y_r}{r}\right)$ are the angles that define the circular segments represented in Fig. 25.

The conditions that must be met in order to use (26) instead of (25) when operating the area $A_3(t)$ are (28) and (29). Note that both equations are modifications on the circle equation: $(x_r - r)^2 \leq r^2 - (y_r - r)^2$.

$$x_r \leq 2 \cdot r - \left(\sqrt{-y_r^2 + 2 \cdot y_r \cdot r} + r\right) \tag{28}$$

$$y_r \leq 2 \cdot r - \left(\sqrt{(-x_r^2 + 2 \cdot x_r \cdot r)} + r\right) \tag{29}$$

If both conditions (28-29) are not met, the projection of the incident light in $A_3(t)$ will be calculated as (25).

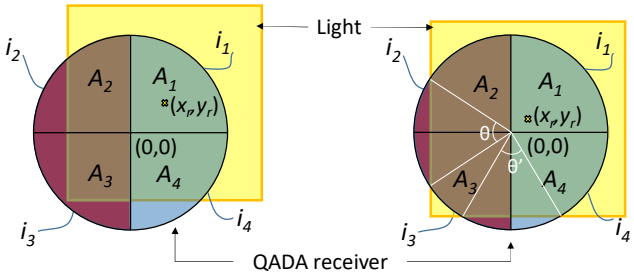


Fig. 25. Projection of the incident light onto the QADA receiver through an aperture for $A_{3,1}(t)$ (left) and $A_{3,2}(t)$ (right).

It can be mentioned that the area $A_1(t)$ depends neither on $x_r$ nor on $y_r$, $A_2(t)$ only depends on $x_r$, $A_4(t)$ only depends on $y_r$, whereas $A_3(t)$ depends both on $x_r$ and $y_r$.

### B. *Enhancement of the proposal considering the polar angle*

This appendix introduces a practical application of the proposal where the receiver is placed on a flat surface (horizontal) and can be rotated an arbitrary polar angle $\beta$ on its $Z$ axis. Consider the same set up as the system presented in Fig. 1 (four LED lamps as transmitters and the QADA receiver analysed in Section III and Appendix A). Once the receiver is illuminated by the LED lamps, and after performing the processing of the QADA output signals (signal correlations, peak detection on the QADA output signals, and calculation of ratios), the incident points of light on the QADA receiver $(x_r, y_r)_i$ are estimated using the algorithm provided in Section III. B. The four impact points $(x_r, y_r)_i$ on the QADA receiver may present a similar shape to the one shown in Fig. 26 a). Note that the four points are equally rotated $\beta$ degrees. After the polar angle $\beta$ is obtained [46], if the incident points on the receiver $(x_r, y_r)_i$ rotate $-\beta$ degrees, they will reach the position $(x_r, y_r)'_i$ presented in Fig. 26 b), equivalent to the case where the receiver has no rotation. At this point, the positioning algorithm continues to obtain the final coordinates $(x, y)$ of the receiver's position in the proposed scenario as discussed in Section IV.

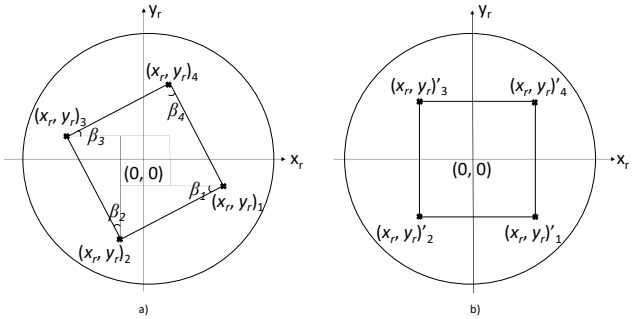


Fig. 26. a) QADA photoreceiver with four rotated impact points $(x_r, y_r)_i$; b) QADA photoreceiver with four non-rotated impact points $(x_r, y_r)'_i$. [46].

## REFERENCES


[1] C. Chen, Y. Han, Y. Chen, and K. J. R. Liu, "Indoor GPS with centimeter accuracy using WiFi," *2016 Asia-Pacific Signal and Information Processing Association Annual Summit and Conference (APSIPA)*, pp. 1-4, 2016.

[2] M. Kovalev, "Indoor positioning of mobile devices by combined Wi-Fi and GPS signals," *2014 International Conference on Indoor Positioning and Indoor Navigation (IPIN)*, pp. 332-339, 2014.

[3] A. Kalbandhe, and S. C. Patil, "Indoor Positioning System using Bluetooth Low Energy," *2016 International Conference on Computing, Analytics and Security Trends (CAST)*, pp. 451-455, 2106.

[4] Á. Parra-Cerrada, V. González-Posadas, J. L. Jiménez-Martín, Á. Blanco-del-Campo, W. Hernandez and C. Calderón-Córdova, "Low-Cost Measurement for a Secondary Mode S Radar Transmitter," in *IEEE Transactions on Instrumentation and Measurement*, vol. 64, no. 12, pp. 3217-3225, Dec. 2015.

[5] J. Ureña, A. Hernández, J. J. García, J.M. Villadangos, M.C. Pérez, D. Gualda, F. J. Álvarez, and T. Aguilera, "Acoustic Local Positioning With Encoded Emission Beacons," *Proceedings of the IEEE*, vol. 106, no. 6, pp. 1042-1062, 2018.

[6] A. Perttula, H. Leppäkoski, M. Kirkko-Jaakkola, P. Davidson, J. Collin and J. Takala, "Distributed Indoor Positioning System With Inertial Measurements and Map Matching," *IEEE Transactions on Instrumentation and Measurement*, vol. 63, no. 11, pp. 2682-2695, Nov. 2014.

[7] Radhamani and B. A. Thomas, "Combined Information Processing of GPS and IMU Sensor using Kalman Filtering," *IJISET - International Journal of Innovative Science, Engineering & Technology*, vol. 3, no. 5, pp. 182-185, May 2016.

[8] A. Lindo, E. Garcia, J. Ureña, M. C. Perez, A. Hernandez, "Multiband waveform design for an ultrasonic indoor positioning system," *IEEE Sensors Journal*, vol. 15(12), pp. 7190-7199, 2015.

[9] M. Scherhäufl, M. Pichler and A. Stelzer, "UHF RFID Localization Based on Evaluation of Backscattered Tag Signals," in *IEEE Transactions on Instrumentation and Measurement*, vol. 64, no. 11, pp. 2889-2899, Nov. 2015.

[10] J. B. Zurn, X. Jiang and Y. Motai, "Video-Based Tracking and Incremental Learning Applied to Rodent Behavioral Activity Under Near-Infrared Illumination," in *IEEE Transactions on Instrumentation and Measurement*, vol. 56, no. 6, pp. 2804-2813, Dec. 2007.

[11] C. Wang, L. Wang, X. Chi, S. Liu, W. Shi, and J. Deng, "The research of indoor positioning based on visible light communication," *China Communications*, vol. 12, no. 8, pp. 85-92, 2015.

[12] T. H. Do, and M. Yoo, "Performance Analysis of Visible Light Communication Using CMOS Sensors," *Sensors*, vol. 16(3), no. 309, pp. 1-23, 2016.

[13] J. Rabadan, V. Guerra, R. Rodríguez, J. Rufo, M. Luna-Rivera, and R. Perez-Jimenez, R., "Hybrid Visible Light and Ultrasound-Based Sensor for Distance Estimation," *Sensors*, vol. 17(2), no. 330, pp. 1-9, 2017.

[14] Q. Huang, Y. Zhang, Z. Ge, and C. Lu, "Refining Wi-Fi Based Indoor Localization with Li-Fi Assisted Model Calibration in Smart Buildings," *Proceedings of the 2016 International Conference on Computing in Civil and Building Engineering*, pp. 1-8, 2015.

[15] N. Rajagopal, P. Lazik, A. Rowe, "Visual light landmarks for mobile devices," *Proceedings of the 13th International Symposium on Information Processing in Sensor Networks,* pp. 249–260, 2014.

[16] G. Simon, G. Zachár and G. Vakulya, "Lookup: Robust and Accurate Indoor Localization Using Visible Light Communication," in *IEEE Transactions on Instrumentation and Measurement*, vol. 66, no. 9, pp. 2337-2348, Sept. 2017.

[17] C. Danakis, M. Afgani, G. Povey, I. Underwood, and H. Haas, "Using a CMOS camera sensor for visible light communication," *Proceedings of the Globecom Workshops (GC Wkshps)*, pp. 1244–1248, 2012.

[18] F. Kazemzadeh, S. A. Haider, C. Scharfenberger, A. Wong and D. A. Clausi, "Multispectral Stereoscopic Imaging Device: Simultaneous Multiview Imaging From the Visible to the Near-Infrared," *in IEEE Transactions on Instrumentation and Measurement*, vol. 63, no. 7, pp. 1871-1873, July 2014.

[19] P. H. Pathak, X. Feng, P. Hu, and P. Mohapatra, "Visible Light Communication, Networking, and Sensing: A Survey, Potential and Challenges," *IEEE Communications Surveys & Tutorials*, vol. 17, no. 4, pp. 2047-2077, 2015.

[20] Y. Cai, W. Guan, Y. Wu, C. Xie, Y. Chen, and L. Fang, "Indoor High Precision Three-Dimensional Positioning System Based on Visible Light Communication Using Particle Swarm Optimization," *IEEE Photonics Journal*, vol. 9, no. 6, pp. 1-20, 2017.

[21] T. Q. Wang, Y. A. Sekercioglu, A. Neild, and J. Armstrong, "Position Accuracy of Time-of-Arrival Based Ranging Using Visible Light With Application in Indoor Localization Systems," *Journal of Lightwave Technology*, vol. 31, no. 20, pp. 3302-3308, 2013.

[22] S. Cincotta, C. He, A. Neild, and J. Armstrong, "High angular resolution visible light positioning using a quadrant photodiode angular diversity aperture receiver (QADA)," *Optics Express*, vol. 26, no. 7, pp. 9230-9242, 2018.

[23] S. H. Yang, H. S. Kim, Y. H. Son, and S. K. Han, "Three-Dimensional Visible Light Indoor Localization Using AOA and RSS With Multiple Optical Receivers," *Journal of Lightwave Technology*, vol. 32, no. 14, pp. 2480-2485, 2014.
[24] G. Berkovic and E. Shafir. "Optical methods for distance and displacement measurements," *Advances in Optics and Photonics,* vol. 4, pp. 441-471, 2012.
[25] S. Cincotta, C. He, A. Neild and J. Armstrong, "Indoor Visible Light Positioning: Overcoming the Practical Limitations of the Quadrant Angular Diversity Aperture Receiver (QADA) by Using the Two-Stage QADA-Plus Receiver," *Sensors,* vol. 19, no. 4: 956, 2019.
[26] S. Cincotta, C. He, A. Neild and J. Armstrong, "QADA-PLUS: A Novel Two-Stage Receiver for Visible Light Positioning," *2018 International Conference on Indoor Positioning and Indoor Navigation (IPIN),* Nantes, 2018, pp. 1-5.
[27] F. Alam, M. T. Chew, T. Wenge and G. S. Gupta, "An Accurate Visible Light Positioning System Using Regenerated Fingerprint Database Based on Calibrated Propagation Model," in *IEEE Transactions on Instrumentation and Measurement*, 2018.
[28] H. Steendam, T. Q. Wang, and J. Armstrong, "Theoretical Lower Bound for Indoor Visible Light Positioning Using Received Signal Strength Measurements and an Aperture-Based Receiver," *Journal of Lightwave Technology*, vol. 35, no. 2, pp. 309-319, 2017.
[29] C. Xie, W. Guan, Y. Wu, L. Fang, and Y. Cai, "The LED-ID Detection and Recognition Method Based on Visible Light Positioning Using Proximity Method," *IEEE Photonics Journal*, vol. 10, no. 2, pp. 1-16, 2018.
[30] Y.S. Eroglu, Y. Yapici, and I. Güvenç, "Impact of Random Receiver Orientation on Visible Light Communications Channel," *CoRR,* 2017.
[31] Z. Li, L. Feng, and A. Yang, "Fusion Based on Visible Light Positioning and Inertial Navigation Using Extended Kalman Filters," *Sensors,* vol. 17, no. 5, pp. 1093, 2017.
[32] M. Ijaz, O. Adebanjo, S. Ansari, Z. Ghassemlooy, S. Rajbhandari, H. Le Minh, A. Gholami and E. Leitgeb, "Experimental Investigation of the Performance of OOK-NRZ and RZ Modulation Techniques under Controlled Turbulence Channel in FSO Systems," *IEEE Transactions on Instrumentation and Measurement*, 2010.
[33] Y. Xu, Z. Wang, P. Liu, J. Chen, S. Han, C. Yu, and J. Yu, "Accuracy analysis and improvement of visible light positioning based on VLC system using orthogonal frequency division multiple access," *Opt. Express*, vol. 25, pp. 32618-32630, 2017.
[34] W. Yu-Lin, H. Chang-Jung, T. Hsin-Mu and L. K. Ching-Ju. "CELLI: Indoor Positioning Using Polarized Sweeping Light Beams," *Proceedings of the 15th Annual International Conference on Mobile Systems, Applications, and Services,* pp. 136-147, 2017.
[35] E. Shinwasusin, C. Charoenlarpnopparut, P. Suksompong and A. Taparugssanagorn, "Modulation performance for visible light communications," *2015 6th International Conference of Information and Communication Technology for Embedded Systems (IC-ICTES)*, pp. 1-4, 2015.
[36] Y. Zhuang *et al*., "A Survey of Positioning Systems Using Visible LED Lights," in *IEEE Communications Surveys & Tutorials*, vol. 20, no. 3, pp. 1963-1988, 2018.
[37] J. Yan, Y. Cheng, K. Lin, D. Chen, C. Chen and K. Feng, "Multipath Interference Free Multi-LED Visible Light Communications with Gold Sequence Multiplexing," *2018 Optical Fiber Communications Conference and Exposition (OFC)*, pp. 1-3, 2018.
[38] J. K. Park, T. Woo, M. Kim and J. T. Kim, "Hadamard Matrix Design for a Low-Cost Indoor Positioning System in Visible Light Communication," in *IEEE Photonics Journal*, vol. 9, no. 2, pp. 1-10, April 2017.
[39] M. Noshad and M. Brandt-Pearce, "Hadamard-Coded Modulation for Visible Light Communications," in *IEEE Transactions on Communications*, vol. 64, no. 3, pp. 1167-1175, March 2016.
[40] Q. Han and H. Lu, "Performance Improvement of Visible Light Communication System Using Reed-Solomon Code," *2015 IEEE 12th Intl Conf on Ubiquitous Intelligence and Computing and 2015 IEEE 12th Intl Conf on Autonomic and Trusted Computing and 2015 IEEE 15th Intl Conf on Scalable Computing and Communications and Its Associated Workshops (UIC-ATC-ScalCom)*, pp. 822-825, 2015.
[41] S. Wan Koo and J. Young Kim, "Performance of double binary turbo coding for visible light communication systems," *2010 The 12th International Conference on Advanced Communication Technology (ICACT)*, pp. 232-237, 2010.
[42] S. Kim and S. Jung, "Novel FEC Coding Scheme for Dimmable Visible Light Communication Based on the Modified Reed–Muller Codes," in *IEEE Photonics Technology Letters*, vol. 23, no. 20, pp. 1514-1516, Oct. 2011.
[43] H. Wang and S. Kim, "Dimming Control Systems With Polar Codes in Visible Light Communication," in *IEEE Photonics Technology Letters*, vol. 29, no. 19, pp. 1651-1654, Oct. 2017.
[44] TT Electronics/Optek Technology, 3 LED Module (30 modules/string) OVM12F3x7 series, www.ttelectronics.com, Issue B, 11/2016, pp. 1-3, Product Specification, 2016.
[45] First Sensor Inc., Series 6 Data Sheet Quad Sum and Difference Amplifier, Part Description QP50-6-18u-SD2, Product Specification, 2012.
[46] E. Aparicio-Esteve, A. Hernández, J. Ureña, J. M. Villadangos and F. Ciudad, "Estimation of the Polar Angle in a 3D Infrared Indoor Positioning System based on a QADA receiver," in *International Conference on Indoor Positioning and Indoor Navigation (IPIN),* pp. 1-8, 2019, doi: 10.1109/IPIN.2019.8911775.
[47] J. R. Barry, "Wireless Infrared Communications," *Kluwer Academic Press*, 1994.
[48] "IEEE Recommended Practices for Modulating Current in High-Brightness LEDs for Mitigating Health Risks to Viewers," in *IEEE Std 1789-2015*, pp. 1-80, June 2015.
[49] C. M. Kuan, "Introduction to econometric theory", Institute of Economics, Academia Sinica, Chapter 7, p. 188, 2000.
[50] Y. S. Eroglu, I. Guvenc, N. Pala and M. Yuksel, "AOA-based localization and tracking in multi-element VLC systems," *2015 IEEE 16th Annual Wireless and Microwave Technology Conference (WAMICON)*, pp. 1-5, 2015.
[51] S. De Lausnay, L. De Strycker, J. Goemaere, N. Stevens and B. Nauwelaers, "A Visible Light Positioning system using Frequency Division Multiple Access with square waves," *2015 9th International Conference on Signal Processing and Communication Systems (ICSPCS)*, Cairns, QLD, 2015, pp. 1-7.
[52] M. Yasir, S. Ho and B. N. Vellambi, "Indoor Position Tracking Using Multiple Optical Receivers," in *Journal of Lightwave Technology*, vol. 34, no. 4, pp. 1166-1176, Feb. 2016.
[53] S. Bastiaens, "Visible Light Positioning using an Aperture based Receiver," Master Thesis, Department of Telecommunications and Information Processing, Ghent University, 2017.
[54] H. Lv, L. Feng, A. Yang, P. Guo, H. Huang and S. Chen, "High Accuracy VLC Indoor Positioning System With Differential Detection," in *IEEE Photonics Journal*, vol. 9, no. 3, pp. 1-13, June 2017.
[55] H. Steendam, "A 3-D Positioning Algorithm for AOA-Based VLP with an Aperture-Based Receiver," *IEEE Journal on Selected Areas in Communications,* vol. 36, no. 1, pp. 23-33, Jan 2018.
[56] A. Arafa, S. Dalmiya, R. Klukas, and J. F. Holzman, "Angle-of-arrival reception for optical wireless location technology," *Opt. Express,* vol. 23, pp. 7755-7766, 2015.

**Elena Aparicio-Esteve** received the B.E.(HONS) degree in Electronic and Electrical Engineering from the Edinburgh Napier University, in 2017, and the B.E. degree in Telecommunication Systems from the Polytechnic University of Cartagena, in 2018. She is currently a Ph.D. candidate in the Electronics Department, University of Alcalá. Her current research areas are local positioning systems and optical communication systems.

**Álvaro Hernández (M'06, SM'15)** received the Ph.D. degree from the University of Alcalá, Spain, and Blaise Pascal University, France, in 2003. He is currently a Professor of Digital Systems and Electronic Design with the Electronics Department, University of Alcalá. His research areas are multisensor integration, electronic systems for mobile robots, and digital and embedded systems.

**Jesús Ureña (M'06, SM'15)** received the B.S. degree in Electronics Engineering and the M.S. degree in Telecommunications Engineering from Universidad Politécnica de Madrid, Spain, in 1986 and 1992, respectively; and the Ph.D. degree in Telecommunications from the Universidad de Alcalá, Spain, in 1998. Since 1986, he has been with the Department of Electronics, University of Alcalá, currently as a Professor. He has collaborated in several educational and research projects in the area of electronic control and sensorial systems for mobile robots and wheelchairs and in the area of electronic distributed systems for railways. His current research interests are in the areas of ultrasonic signal processing, local positioning systems (LPSs) and activity monitoring, and sensory systems for railway safety.

**José M. Villadangos** received the Ph.D. degree from the University of Alcala, Alcalá de Henares, Spain, in 2013. He is currently an Associate Professor of Electronic Digital Systems with the Electronics Department, University of Alcala. His current research interests include multisensor integration, electronic systems for mobile robots, digital and embedded systems, low-level ultrasonic signal processing, and local positioning systems.